

Scaling laws governing the erosion and impact resistance of thermal barrier coatings

A.G. Evans^{a,*}, N.A. Fleck^b, S. Faulhaber^a, N. Vermaak^a, M. Maloney^c, R. Darolia^d

^a *Materials Department, University of California, Santa Barbara, CA 93106-5050, USA*

^b *Cambridge University Engineering Department, Trumpington Street, Cambridge CB2 1PZ, UK*

^c *Pratt & Whitney, East Hartford, CT 06108, USA*

^d *GE Aircraft Engines, Cincinnati, OH 45215, USA*

Received 29 April 2004; received in revised form 22 April 2005; accepted 19 May 2005

Available online 8 August 2005

Abstract

Airfoils coated with columnar thermal barriers have been removed from aero-engines and characterized. Observations of deformation and cracking have been used to identify three material removal mechanisms. These are: (i) sub-surface, trans-columnar cracking attributed to the initial elasto-dynamic response (nanosecond timeframes), (ii) segmented cone cracks when the ensuing penetration (millisecond timescale) remains elastic, (iii) local densification, accompanied by either kink bands or lateral cracks when the projectile penetrates plastically, especially at high temperature. Basic impact mechanics, combined with fracture criteria, have been used to devise scaling laws for these mechanisms. The results are combined to derive relations that characterize the thresholds for material removal and the transitions between major mechanisms (expressed in terms of a mechanism map). Some aspects of the material removal at kinetic energies above the thresholds are examined.

© 2005 Elsevier B.V. All rights reserved.

Keywords: Aero-engines; Cracking; Trans-columnar cracking; Elasto-dynamic response; Deformation; Airfoils; Densification

1. Introduction

Thermal barrier systems used in gas turbines exhibit two major categories of failure: one based on oxidation [1–10] and the other on impact by projectiles ingested into the gas stream [11–15]. Both categories have been subject to a combination of experimental assessment and modeling. The models of oxidation-induced failure have reached a maturity that allows trends with constituent properties to be ascertained [9]. The situation is much less mature for failure mechanisms caused by impact. The intent of this article is to develop and pursue a protocol for establishing connections between material removal rates caused by particle impact and the properties of the thermal barrier material. The assessment is confined to materials deposited using electron beam physical vapor

deposition (EB-PVD), which have a columnar microstructure (Figs. 1–3).

Progress toward a mechanistic understanding has been limited by the absence of well-controlled experiments capable of duplicating the conditions expected in turbine engines. The challenges are associated with the high temperatures (typically 1100 °C) and high impact velocities (up to 300 m/s), as well as the relatively small particles involved (20–500 μm) and their composition (usually calcium-magnesium-alumino-silicate: CMAS). Presently, there are no systems capable of single particle impacts that function in this parameter range. Instead, to provide insight, the following have been used: (i) engine hardware impacted by CMAS particles [16], (ii) burner rig specimens impacted at high temperature by alumina particles [13,14] and (iii) erosion rigs at lower temperatures [11,12]. In such tests, the size and velocity of the impacting particles responsible for specific damage sites are unknown. Moreover, when engine hardware is used, the temperature of the surface during impact is also unknown.

* Corresponding author.

E-mail address: agevans@engineering.ucsb.edu (A.G. Evans).

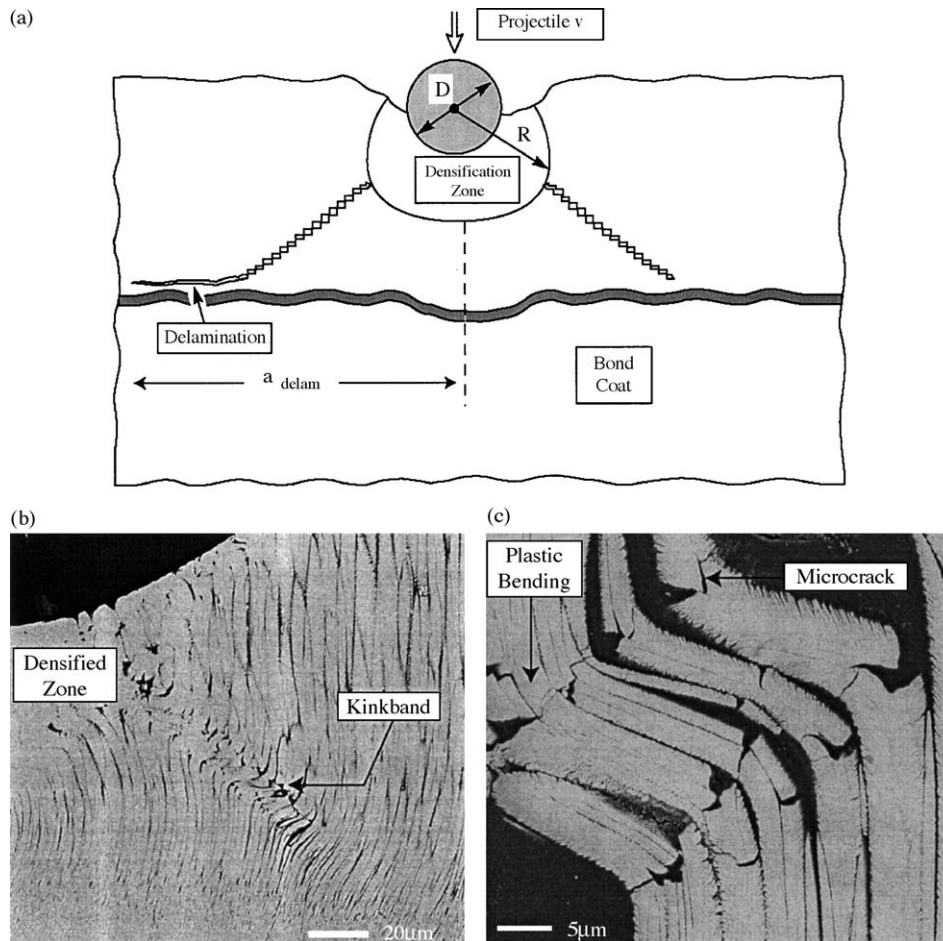


Fig. 1. For impact conditions above a plasticity threshold, the material deforms and densifies, accompanied by kink bands, which extend diagonally downward and, in some cases, induce delaminations along the interface with the TGO. The process occurs over several milliseconds: (a) schematic, (b) and (c) scanning electron microscope images of cross sections of a 7YSZ subjected to plastic penetration at 1150 °C [17].

Subject to these limitations, a strategy is needed that provides insight and understanding about mechanisms and ensuing trends with constituent properties.

The strategy to be pursued integrates observations with scaling analyses. Namely, cross sections are made on airfoils exposed to particle impacts, and collages of observations are used to categorize the mechanisms responsible for the cracks and other disturbances. Particle impact analyses are conducted in parallel. The expectation is that, by relating the calculated stresses, displacement fields and energy release rates to the observations, the most important mechanisms of material removal will be elucidated. Thereafter, by developing mechanism-based scaling relations, trends in material removal with constituent properties and microstructure might be established. In turn, the trends will be used to guide the development of materials with potential for diminished erosion. The ultimate goal will be to corroborate the mechanisms by testing and fielding new materials, facilitated by full-scale simulations.

The present article is organized as follows. A synopsis is presented of the mechanisms that have been surmised

from previous assessments [11–18], accompanied by additional observations of impact-induced phenomena, ascertained from cross sections of airfoils removed from aero-engines. Based on these insights, some basic penetration mechanics are summarized and used to establish formulae that relate the forces, stresses and penetrations to the kinetic energy of the impact. A mapping scheme is devised that provides a basis for further assessments. The results are combined in a manner that enables the derivation of scaling relations that characterize: (a) the thresholds for material removal, (b) the transitions between major mechanisms (expressed in terms of a mechanism map) and (c) some aspects of material removal at kinetic energies above the thresholds.

To facilitate the presentation, non-dimensional parameters are defined. The parameters refer to an impacting particle with diameter $D=2R$, density ρ_p , Young's modulus E_p . The TBC is characterized by an intra-columnar Young's modulus E_{tbc} , uniaxial yield strength σ_Y , density ρ_{tbc} and thickness H . At instantaneous penetration depth δ , the current contact load is P , and the particle velocity v . The ensuing non-dimensional

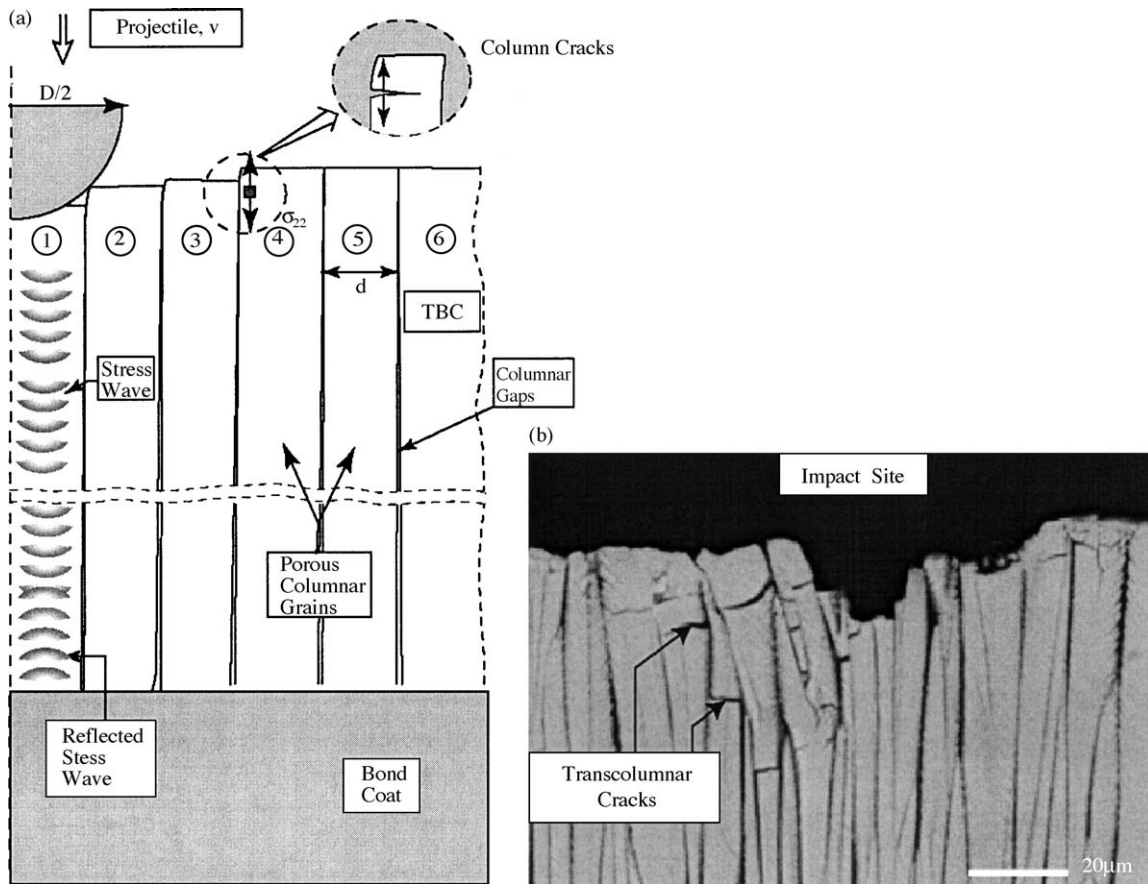


Fig. 2. In all cases, upon initial impact, stress waves emerge from the impact site. One set is manifest as bending waves that extend just beneath the surface causing tensile stress in the columns. Above a threshold, these stresses cause trans-columnar cracks that result in material removal. The process occurs over several nanoseconds: (a) schematic and (b) scanning electron microscope image of cross section of 7YSZ airfoil within an eroded region.

groups are:

$$\bar{P} \equiv \frac{P}{R^2 E_{\text{tbc}}}$$

$$\bar{v} \equiv v \sqrt{\rho_{\text{p}} / E_{\text{tbc}}}$$

$$\bar{\delta} \equiv \frac{\delta}{H}$$

$$\varepsilon_{\text{Y}} \equiv \frac{\sigma_{\text{Y}}}{E_{\text{tbc}}}$$

Note that the non-dimensional velocity can be equally phrased as v/c with $c \equiv \sqrt{E_{\text{tbc}}/\rho_{\text{tbc}}}$ the elastic wave speed. Moreover, the thresholds, mechanism transitions and material removal can all be expressed in terms of the geometry H/R and two additional non-dimensional parameters: one related to the TBC toughness, Γ_{tbc} , and a second to the column diameter, d . The parameters are:

$$\Pi = \frac{\Gamma_{\text{tbc}}}{E_{\text{tbc}} D} \quad \mathcal{E} = \frac{d}{D}$$

All of the results will be expressed in terms of these parameters.

2. Synopsis of mechanisms

Previous activities have suggested plastic damage mechanisms, as depicted in Fig. 1, and elasto-dynamic mechanisms as depicted in Fig. 2. Consider each in turn.

2.1. Plastic damage mechanisms

Combinations of large kinetic energy and high temperature cause the material to be susceptible to large-scale plastic deformation and densification around the contact site (Fig. 1). The deformation zones develop over millisecond timescales, as the impacting particle decelerates [14,15]. Outside the densified zone, kink bands form and extend diagonally downward, toward the interface with the thermally grown oxide (TGO) (Fig. 1). Within the bands, the columns are plastically bent, causing the boundaries of the kink band to crack, and thereby weakening the material. Similar responses have been observed during quasi-static penetration at elevated temperature [17,18]. The similarity between impact and indentation indicates that the plasticity-based mechanisms governing material removal are not strongly affected by strain rate. In some cases, the bands reach the interface with the thermally

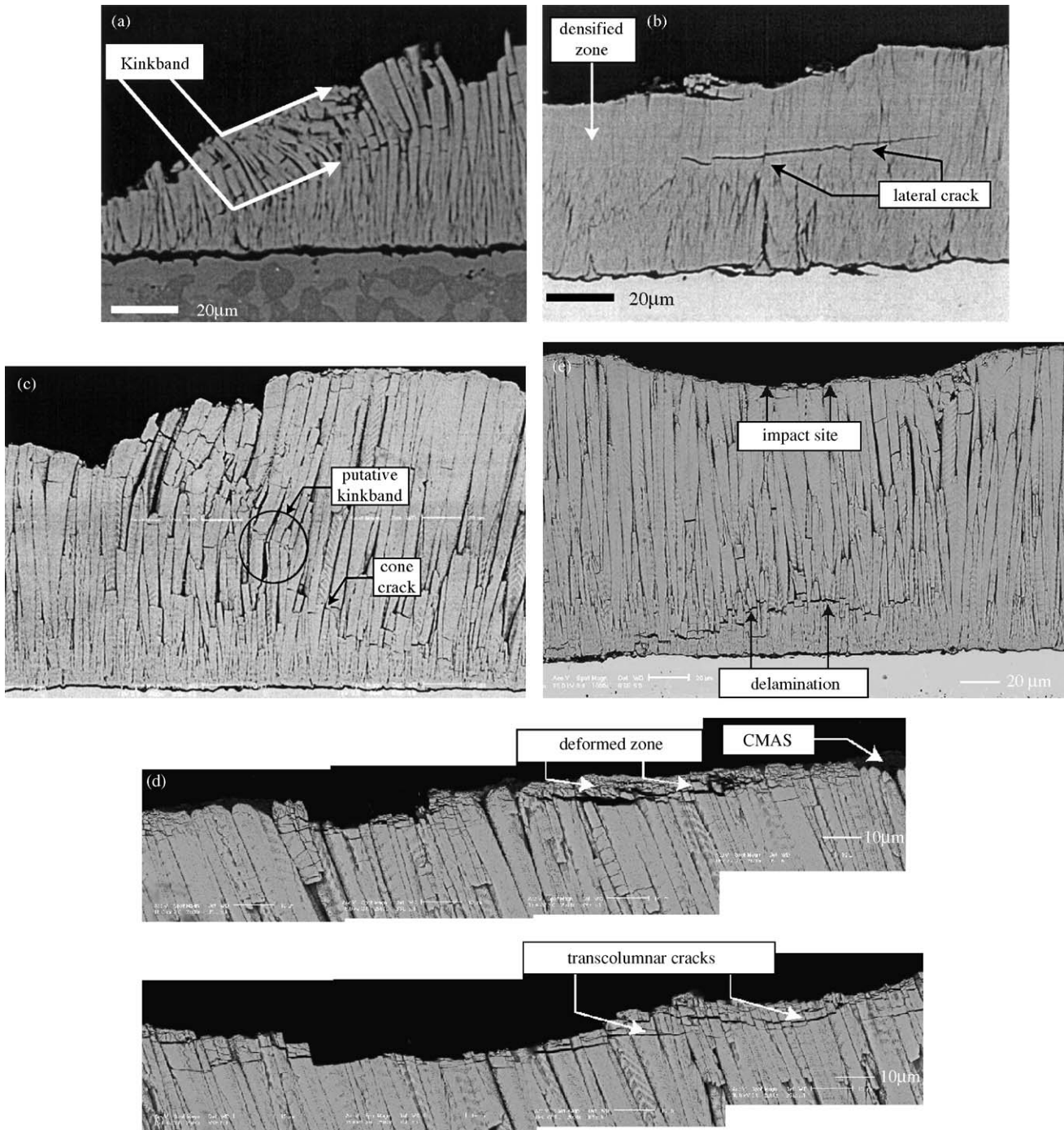


Fig. 3. Scanning electron microscope images of cross sections from airfoils, (a) oblique kink band showing material removed above the upper plane [16]; (b) example of a lateral crack beneath a densified zone; (c) a segmented cone crack with a small area (circled) suggestive of a putative kink band; (d) a region near the tops of the columns with multiple trans-columnar cracks: at the very top, above the cracks, the material appears to be deformed or sintered; (e) a delamination just above the TGO associated with a large crater: otherwise the response appears elastic (that is, no densification and no plastic bending). It is suggested that the crack is caused by a reflected elastic wave [15].

grown oxide. When this happens, they nucleate a delamination that extends outward from the impact site, along a trajectory within the TBC, just above the TGO. Such delaminations provide a mechanism for creating large-scale spalls [14].

2.2. Elasto-dynamic mechanisms

During initial impact, elastic waves are induced that interact with flaws in the columns (Fig. 2). Within nanoseconds, bending waves propagate at the tops of the columns to

accommodate the projectile as it penetrates [15]. The localized bending causes trans-columnar cracks beneath the surface. The ensuing array, upon linkage (Fig. 2), causes small amounts of material to be removed. Elastic waves also reflect off the bottom of the columns [15], becoming tensile waves that propagate back to the surface. The timescale is in the order of 60 ns. These waves may also cause cracks to form and extend across the columns.

3. Observations on airfoils

Airfoils removed from service that have experienced some material loss by erosion and/or FOD have been cross sectioned and examined by scanning electron microscopy. The sectioning methods have been described elsewhere [3]. A selection of the cracking phenomena found in these investigations is presented in Fig. 3. Four different cracking responses are apparent, indicative of mechanisms both supportive of and additional to those in Figs. 1 and 2.

- (i) The image in Fig. 3a represents the occasional observation that kink bands form, followed by removal of material above the upper, bounding plane [16].
- (ii) The image in Fig. 3b reveals a densified zone, similar to that in Fig. 1, but there is no kink band. Instead, a crack is apparent just beneath the dense zone, extending parallel to the surface. Such cracks are reminiscent of lateral cracks that form upon plastic indentation of monolithic ceramics (Fig. 4a) [20,23].
- (iii) The image in Fig. 3c appears to resemble the Hertzian (cone) cracks that form when a ceramic responds to a slow elastic impact (Fig. 4b) [19]. However, in the highlighted area, it also has features indicative of a putative kink band. In the ensuing discussion, these are treated as segmented cone cracks arising from a predominantly elastic response.
- (iv) The image in Fig. 3d indicates a multiplicity of trans-columnar cracks confined to a small region beneath the eroded surface. The number density of the cracks is much higher than that depicted in Fig. 2. There is also evidence of a thin surface layer that appears to have been fragmented and, thereafter, either deformed or sintered. This mechanism may be a variant on the elasto-dynamic response (Fig. 2). Another observation (Fig. 3e) suggests a delamination caused by a stress wave reflected from the TGO.

In summary, the new observations affirm the three following fundamental mechanisms and suggest others. (i) Plastic damage (Fig. 1) manifest as densification accompanied either by a kink band (Fig. 1) or by a lateral crack (Fig. 3b), (ii) sparse trans-columnar cracks caused by elastic stress waves (Fig. 2) and (iii) segmented cone cracks due to elastic penetration (Fig. 3c). Additional mechanisms are exemplified by the dense trans-columnar cracks (Fig. 3d) and delaminations close to the TGO (Fig. 3e).

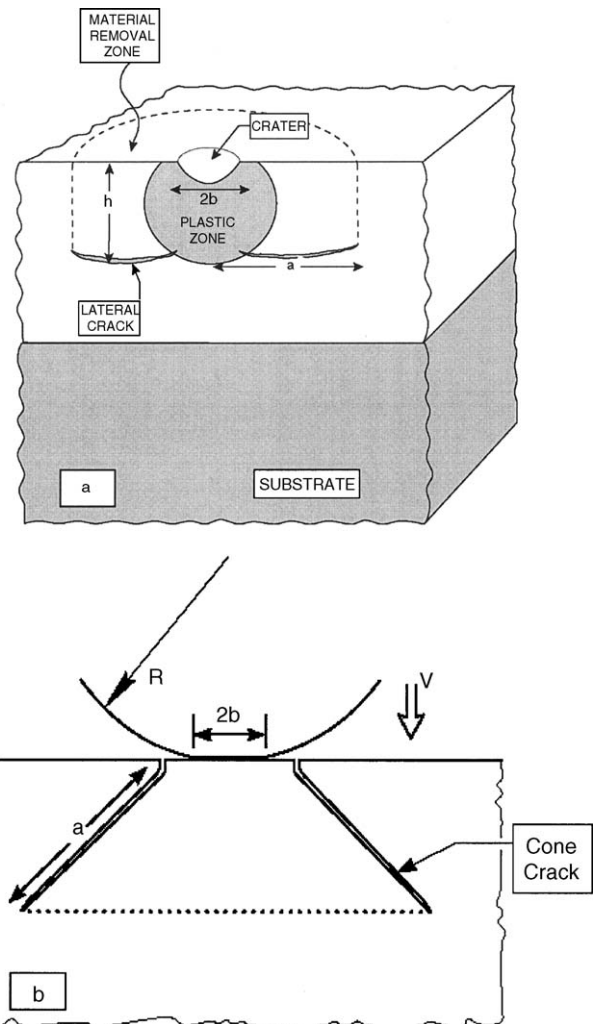


Fig. 4. Schematics of two types of crack: (a) lateral crack beneath a plastic zone and (b) a Hertzian crack.

4. Penetration mechanics

The response of the TBC to normal impact by a spherical particle can be used to construct a mechanism map (Fig. 5) that facilitates understanding of the basic domains. Most of the background results reside in standard texts on penetration [19] and indentation [20]. Others are described in a recent article [21], with the basic formulae therefrom summarized in Appendix A. Three basic regimes are addressed, (a) *Elasto-dynamic contact*: that is, elastic wave emission occurs upon initial contact in nanosecond time frames. Thereafter, over milliseconds, either (b) *quasi-static elastic* or (c) *plastic contact* develop and evolve. The assessment assumes that a 1D analysis approximates the response of a columnar microstructure. Penetrations much smaller than the particle radius R are considered, such that the contact radius: $b \approx \sqrt{2R\delta}$. By using the results in Appendix A, the mechanism maps presented in Fig. 5 have been constructed for a TBC thickness, $H = 100 \mu\text{m}$. They are for representative val-

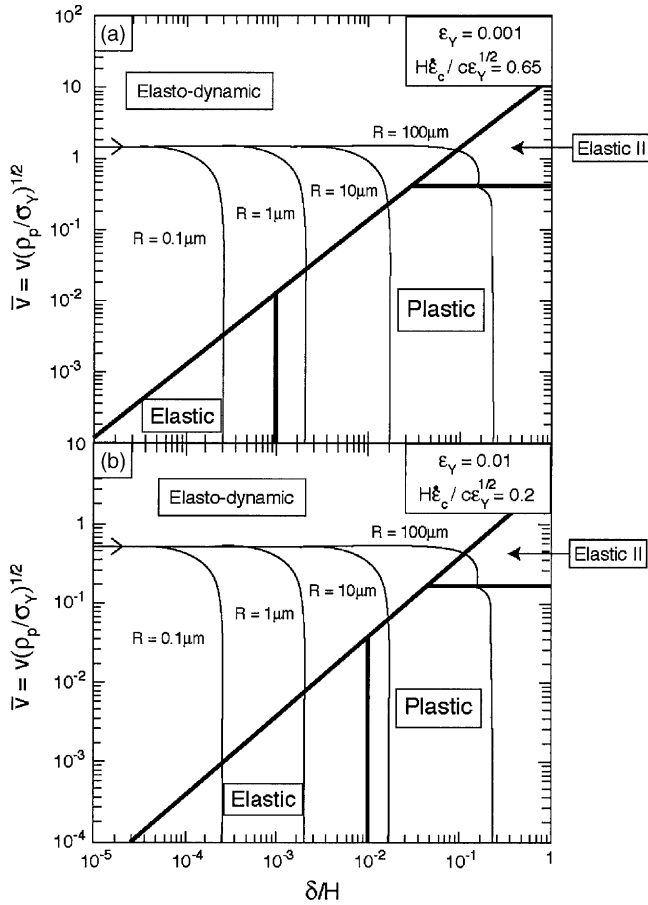


Fig. 5. Mechanism maps for the response of a TBC to high velocity projectile impact, with penetration trajectories superposed. The elastic domain at the upper right corner arises because plasticity is suppressed at very high strain rates. (a) A map for a soft TBC ($\varepsilon_Y = 0.001$) showing that, while the initial contact is elastodynamic, eventually, before the projectile arrests, the contact becomes plastic. The exception is the response to very small projectiles, which remains elastic throughout; (b) a map for a harder TBC ($\varepsilon_Y = 0.01$) showing that the initial contact is again elastodynamic, but thereafter, the TBC remains elastic.

ues of the yield strain: $\varepsilon_Y = 0.001$ (Fig. 5a) and 0.01 (Fig. 5b). Velocity/penetration trajectories are superposed. Beyond the *elasto-dynamic* phase (ending at, $t_{\text{end}} = 2H/c$), the response to deeper penetrations depends on v/H and $\delta/2H$. It is elastic whenever $v/H > 10^6/s$ and $\delta/2H < \varepsilon_Y$ and plastic when $v/H < 10^6/s$ and $\delta/2H > \varepsilon_Y$.

The main implications are straightforward. For materials with relatively low yield strain ($\varepsilon_Y = 0.001$, Fig. 5a), impacted by relatively large particles, trajectories that start in the elasto-dynamic domain transition into the plastic range. For such impacts, the elasto-dynamic mechanism (Fig. 2) operates first (in ns timescale), followed by the plastic damage mechanism (ms timescale) depicted in Fig. 1. In such cases, erosion and FOD would be dominated by the larger scale damage created during plastic penetration. That is, the elasto-dynamic phase can be neglected. The ensuing consequences are described below.

For materials with higher yield strain ($\varepsilon_Y = 0.01$, Fig. 5b), or for impacts by smaller particles, the contact remains elastic throughout. In such cases, the elasto-dynamic mechanism would apply initially, followed at the higher levels of kinetic energy by a more damaging cone crack mechanism. The ensuing emphasis is on the latter.

5. Mechanics of cracking

5.1. Elasto-dynamic cracking

The incidence of trans-column cracking (Fig. 2) during the initial, elasto-dynamic stage of the impact is dependent on the non-dimensional parameter [15]:

$$\Theta \equiv \frac{P_{\text{max}}^2 a_0}{E_{\text{tbc}} \Gamma_{\text{tbc}}} \quad (1)$$

where a_0 is the size of pre-existent cracks in the columns. To interpret this formula, recall that cracks form when Θ exceeds a critical value, Θ_c [15]. Take the maximum contact pressure to be $p_{\text{max}} = v_0 \sqrt{E_{\text{tbc}} \rho_{\text{tbc}}}$ in terms of the initial particle velocity v_0 , as discussed in Appendix A. Upon assuming that a_0 scales with the column diameter, d , the threshold velocity of the particle becomes:

$$\bar{v}_{\text{th}} = \sqrt{\frac{\Theta_c \Pi}{\varepsilon}} \quad (2)$$

5.2. Plastic damage

When the penetration becomes plastic (Fig. 5), several forms of damage can ensue (Figs. 1 and 3b). A crater forms having volume:

$$\frac{V_{\text{crater}}}{D^3} = 0.174\pi(C\varepsilon_Y)^{-3/4} \bar{v}_0^{3/2} \quad (3)$$

The volume is accommodated by densification. Material loss is caused either by delamination induced by shear bands (Fig. 1) or by lateral cracks (Fig. 4b). Presently, only the lateral crack mechanism has received sufficient analysis to derive scaling relationships [20,24]: with preliminary results for shear bands [25]. Such analysis provides the following relationships.

5.2.1. The threshold

Before cracks can be induced at the crater (Figs. 4a and 3c), a threshold condition must be exceeded, comparable to that for lateral crack nucleation at quasi-static indentations [20,23]. The scaling is expressed by the non-dimensional index [15,20]:

$$\Delta = \frac{\sigma_Y \sqrt{h_{\text{pl}}}}{\sqrt{E_{\text{tbc}} \Gamma_{\text{tbc}}}} \quad (4)$$

where h_{pl} is the depth of plastic zone, as specified by (A.10). Experimental observations on monolithic ceramics indi-

cate that dominant lateral cracks form when $\Delta_{th} \geq 3 \times 10^{-3}$ [20]. Combining with (A.9) and (A.10), the threshold index becomes:

$$\bar{v}_{th} = 4\sqrt{1.5C\varepsilon_Y^{-7/2}}\Pi^2\Delta_{th}^4 \quad (5)$$

5.2.2. Crack extension

When the impact conditions result in *shallow penetration* of the plastic zone, cracks can form at its base and extend laterally, entirely within the TBC (Fig. 4a). The delamination radius scales as [24]:

$$\frac{a_{delam}}{h} \approx \frac{0.3W_{pl}}{\sqrt{E_{tbc}\Gamma_{tbc}h^{5/2}}} \quad (6)$$

where h is the depth of the crack below the surface and W_{pl} is the plastic work done by the projectile as it penetrates. Noting that cracks usually form at the base of the plastic zone [20,23], upon equating h to h_{pl} (A.10) and incorporating the plastic work during penetration (A.11), the delamination radius becomes:

$$\frac{a_{delam}}{D} = \frac{0.1\pi}{\sqrt{2}}(1.5C\varepsilon_Y)^{3/8}\frac{\bar{v}^{5/4}}{\Pi^{1/2}} \quad (7)$$

5.3. Segmented cone cracking

Basic results from penetration mechanics [19] can be used to demonstrate that the maximum force exerted on an isotropic elastic substrate by an impacting sphere is:

$$\bar{P}_{max}^5 = 2.1\pi^3\bar{v}^6 \quad (8)$$

Moreover, the *threshold for cone cracking* has been ascertained [20] and given by:

$$P_{th} = \beta\Gamma_{tbc}R \quad (9a)$$

or

$$\bar{P}_{th} = 2\beta\Pi \quad (9b)$$

where, $\beta = 2.5 \times 10^5$. Combining (8) and (9a) and (9b) gives a threshold velocity:

$$\bar{v}_{th} = \left[\frac{(2\beta)^5}{2.1\pi^3} \right]^{1/6} \Pi^{5/6} \quad (10)$$

Above the threshold, the length of the cone cracks has the form [20]:

$$\left(\frac{a_{cone}}{D} \right)^{3/2} = \kappa \left[\frac{\bar{P}}{\Pi^{1/2}} \right] \quad (11a)$$

where $\kappa = 10^{-4}$. Inserting the maximum load from (8):

$$\frac{a_{cone}}{D} = 1.1\pi^{2/5}\kappa^{2/3}\frac{\bar{v}_0^{4/5}}{\Pi^{1/3}} \quad (11b)$$

6. Scaling relations

To design an erosion resistant material, the highest priority is to seek a material property combination that completely eliminates cracking. The salient cracking thresholds are affected by *the transition from elastic-to-plastic penetration*. The non-dimensional velocity at the transition, \bar{v}_{tr} , above which the TBC exhibits plastic deformation is obtained from (A.4) and (A.5), upon equating $p = \sigma_Y$, as:

$$\bar{v}_{tr} \approx 2 \left(\frac{H}{R} \right) \varepsilon_Y^{3/2}$$

That is, plastic deformation occurs whenever, $\bar{v} \geq \bar{v}_{tr}$. In general, a plastic (rather than elastic) response is preferred, because then, an appreciable fraction of the kinetic energy of the impinging particle is converted to plastic dissipation, diminishing the damage.

6.1. Erosion thresholds

For trans-columnar cracking at short times (2):

$$\bar{v}_{elth} = \sqrt{\frac{\Theta_c\Pi}{\mathcal{E}}}$$

For lateral cracking at longer times, when $\bar{v} \geq \bar{v}_{tr}$ (5):

$$\bar{v}_{th} = 4\sqrt{1.5C\varepsilon_Y^{-7/2}}\Pi^2\Delta_{th}^4$$

For segmented cone cracking at longer times, when $\bar{v} \leq \bar{v}_{tr}$ (10):

$$\frac{V_{crater}}{D^3} = 0.174\pi(C\varepsilon_Y)^{-3/4}\bar{v}_0^{3/2}$$

There is also a threshold for forming kink bands [25], but its explicit dependence on material properties remains to be ascertained.

The preceding results can be plotted in the form of a *mechanism map* in three-dimensional (\bar{v}_0 , ε_Y , Π) space (Fig. 6). The map identifies the combination of material properties that resist cracking for specified impacts. Note that, in all cases, the onset of cracking is suppressed by a high TBC toughness (manifest in the trend with $\Pi = \Gamma_{tbc}/E_{tbc}D$). The map also reveals that, for two reasons, the yield strain at high temperature (1100 °C), ε_Y , should be as small as possible. (a) According to (A.12), lowering ε_Y decreases the velocity at the plasticity transition, diminishing the damage, (b) moreover, once plastic, the threshold energy, \bar{v}_{th} , increases as ε_Y decreases. For more quantitative application, the scaling coefficients must be established, either by experiment or by a more comprehensive model. Ascertaining these coefficients provides a focus for ongoing research.

Determination of the *material removal rates* above the thresholds remains incomplete. Relevant results include the delamination size when $\bar{v} \geq \bar{v}_{tr}$ (7):

$$\frac{a_{delam}}{D} = \frac{0.1\pi}{\sqrt{2}}(1.5C\varepsilon_Y)^{3/8}\frac{\bar{v}^{5/4}}{\Pi^{1/2}}$$

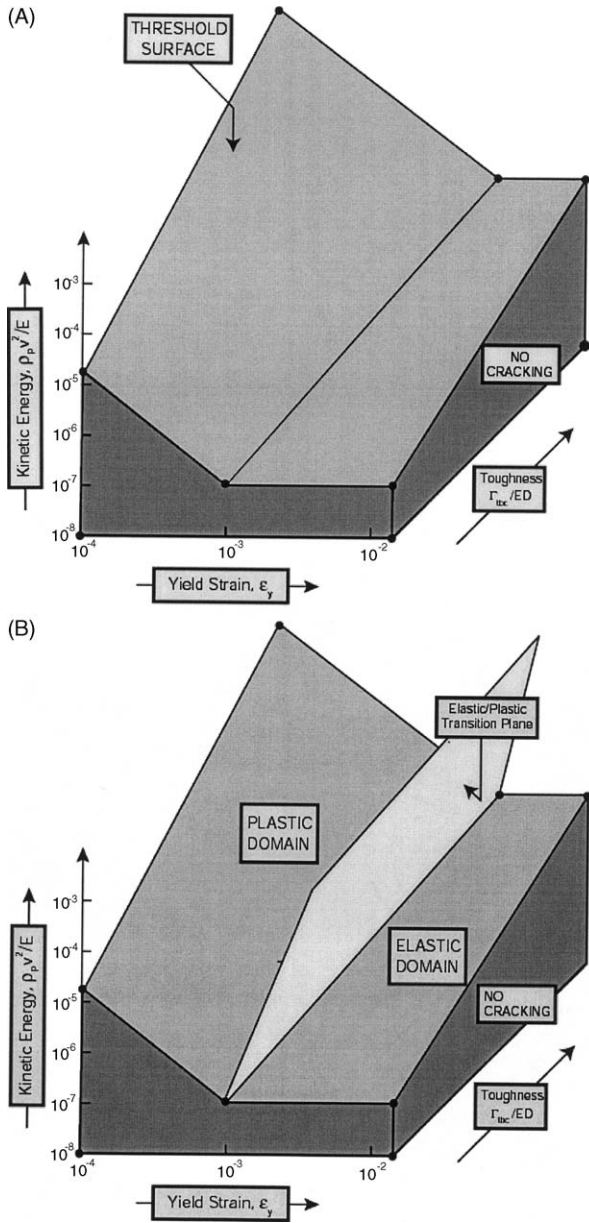


Fig. 6. Mechanism maps for the onset of material removal by particle impact. The coordinates are: $\bar{v}_0^2 = \frac{\rho_p v^2}{E_{tbc}}$, $\Pi = \frac{\Gamma_{tbc}}{E_{tbc} D}$, ϵ_Y . (a) The threshold surface indicating the domain (below this surface) wherein cracks should not be formed; (b) the same threshold surface as in (a) with the plane indicating the transition from elastic to plastic response superposed, for the choice $H/R = 5$.

as well as the cone crack size when $\bar{v} \leq \bar{v}_{tr}$ (11a) and (11b):

$$\frac{a_{cone}}{D} = 1.1\pi^{2/5} \kappa^{2/3} \frac{\bar{v}_0^{4/5}}{\Pi^{1/3}}$$

and the crater size when $\bar{v} \geq \bar{v}_{tr}$ (3):

$$\frac{V_{crater}}{D^3} = 0.89 \left(\frac{\pi}{12}\right)^{3/4} \bar{v}_0^{3/4} \epsilon_Y^{3/8}$$

These results alone do not provide much insight beyond demonstrating the expected benefit of higher toughness and

specifying the velocity exponents. To ascertain erosion rates, additional mechanistic information must be pursued.

7. Implications and conclusion

The preceding scaling analysis provides some basic insight about the relative importance of the properties of the TBC having the greatest influence on erosion. As expected, elevating the TBC toughness has the most pervasive influence, especially through its role in elevating the cracking threshold. The corresponding role of the TBC yield strength (or hot hardness) is not transparent without guidance from models. The implication from the models is that softer materials (at high temperature) should have a substantially higher cracking threshold. This prediction will be tested by comparing the erosion trends among TBCs with different high temperature penetration resistance [17,25]. Note, however, that for softer TBCs, the craters would be deeper. This would not be a problem for normal impacts, since there is no material removal below the cracking threshold. But cratering could adversely affect the material loss if a plastic plowing mechanism were to operate when the particles arrive at high obliquity. Such behavior would be similar to that found in metals, which erode more rapidly when their hardness is diminished [26].

Appendix A. A synopsis of penetration mechanics formulae [21]

The *elastic waves* travel at a velocity, $c \equiv \sqrt{E_{tbc}/\rho_{tbc}}$, resulting in a pressure, $p_{ed} = \sqrt{E_{tbc}\rho_{tbc}}v$. The non-dimensional contact force is [21]:

$$\bar{P}_{ed} = 2\pi \sqrt{\frac{\rho_{tbc}}{\rho_p}} \frac{H}{R} \bar{v} \bar{\delta} \quad (A.1)$$

Equating this force to the product of particle mass and acceleration, and integrating with respect to δ gives the velocity change:

$$\Delta \bar{v}_{ed} = -\frac{3}{4} \sqrt{\frac{\rho_{tbc}}{\rho_p}} \left(\frac{H}{R}\right)^2 [\Delta \bar{\delta}^2] \quad (A.2)$$

This elasto-dynamic phase ends when:

$$t_{end} = \frac{2H}{c} \quad (A.3)$$

when the ensuing response is *quasi-static elastic*, the force, P , and average contact pressure, p , exerted by the particle are [21]:

$$\bar{P} = \pi \frac{H}{R} \bar{\delta}^2 \quad p = \frac{E_{tbc} \delta}{2H} \quad (A.4)$$

The velocity/penetration relation is:

$$\Delta(\bar{v}_{el}^2) = -\frac{1}{2} \left(\frac{H}{R}\right)^2 \Delta(\bar{\delta}^3) \quad (A.5)$$

such that the maximum penetration is:

$$\bar{\delta}_{\max}^3 = 2 \left(\frac{R}{H} \right)^2 \bar{v}_0^2 \quad (\text{A.6})$$

in terms of the initial particle velocity \bar{v}_0 .

Alternatively, should the contact become *plastic*, the contact force is related to the impression depth by [22]:

$$\bar{P}_p = 2\pi C \left(\frac{H}{R} \right) \bar{\delta} \varepsilon_Y \quad (\text{A.7})$$

where the constraint factor: $C \approx 2$. The velocity change becomes:

$$\Delta(\bar{v}_{\text{pl}}^2) = -1.5C \left(\frac{H}{R} \right)^2 \varepsilon_Y [\Delta(\bar{\delta}^2)] \quad (\text{A.8})$$

The maximum penetration is [14,19]:

$$\bar{\delta} = \frac{1}{\sqrt{1.5C\varepsilon_Y}} \frac{R}{H} \bar{v}_0 \quad (\text{A.9})$$

The depth, h_{pl} , of the plastic zone scales with the penetration as [14]:

$$h_{\text{pl}} \sim \sqrt{\delta_{\max} R} \quad (\text{A.10})$$

The plastic work of penetration is:

$$W_{\text{pl}} = 2\pi C R \sigma_Y \int_0^{\delta_{\max}} \delta d\delta = \frac{2\pi}{3} E_{\text{tbc}} R^3 \bar{v}_0^2 \quad (\text{A.11})$$

Mechanism maps can be constructed from these formulae by using the instantaneous values of $\bar{\delta}$ and \bar{v} (Fig. 5). The additional non-dimensional groups (ρ_p/ρ_{tbc} , ε_Y , H/R) must be specified independently. The boundaries between competing mechanisms are located by equating $\bar{\delta}$ and \bar{v} for the mechanisms on each side. *The elastic/plastic boundary* occurs at penetration:

$$\bar{\delta}_{\text{e/p}} = \varepsilon_Y \quad (\text{A.12})$$

The elastic/elasto-dynamic boundary (for $\rho_p/\rho_{\text{tbc}} = 1$) occurs at:

$$\bar{\delta}_{\text{e/ed}} = 2\bar{v}_0 \quad (\text{A.13})$$

References

- [1] A.G. Evans, D.R. Mumm, J.W. Hutchinson, G.H. Meier, F.S. Pettit, *Prog. Mater. Sci.* 46 (2001) 505.
- [2] J.A. Ruud, A. Bartz, M.P. Borom, C.A. Johnson, *J. Am. Ceram. Soc.* 84 (2001) 1545.
- [3] T. Xu, S. Faulhaber, C. Mercer, M. Maloney, A. Evans, *Acta Mater.* 52 (2004) 1439–1450.
- [4] N. Padture, M. Gell, E. Jordan, *Science* 296 (2002) 280.
- [5] M.J. Stiger, N.M. Yanar, M.G. Toppings, F.S. Pettit, G.H. Meier, *Z Metallkd.* 90 (1999) 1069.
- [6] J.M. Ambrico, M.R. Begley, E.H. Jordan, *Acta Mater.* 49 (2001) 1577.
- [7] A.M. Karlsson, J.W. Hutchinson, A.G. Evans, *J. Mech. Phys. Solids* 50 (2002) 1565.
- [8] D.R. Mumm, M. Watanabe, A.G. Evans, J.A. Pfaendtner, *Acta Mater.* 52 (2004) 1123.
- [9] T. Xu, M.Y. He, A.G. Evans, *Acta Mater.* 51 (2003) 3807.
- [10] V. Tolpygo, D.R. Clarke, *Acta Mater.* 48 (2000) 3283.
- [11] J.R. Nicholls, M.J. Deakin, D.S. Rickerby, *Wear* 23 (1999) 352.
- [12] R.G. Wellman, J.R. Nicholls, *Wear* 242 (2000) 89.
- [13] R.W. Bruce, *Tribol. Trans.* 41 (1998) 399.
- [14] X. Chen, R. Wang, N. Yao, A.G. Evans, J.W. Hutchinson, R.W. Bruce, *Mater. Sci. Eng. A352* (2003) 221.
- [15] X. Chen, N.A. Fleck, I. Spitsberg, A.G. Evans, J.W. Hutchinson, *Wear* 256 (2004) 735–746.
- [16] M.J. Maloney, R. Darolia, unpublished observations.
- [17] M. Watanabe, C. Mercer, C.G. Levi, A.G. Evans, *Acta Mater.* 52 (2004) 1479–1487.
- [18] X. Chen, J.W. Hutchinson, A.G. Evans, *Acta Mater.* 52 (2004) 565–571.
- [19] K.L. Johnson, *Contact Mechanics*, Cambridge University Press, Cambridge, 1985.
- [20] B.R. Lawn, *Fracture of Brittle Solids*, Cambridge University Press, 1975.
- [21] N.A. Fleck, Z. Thanasis, in press.
- [22] A.F. Bower, N.A. Fleck, A. Needleman, N. Ogbonna, *Proc. R. Soc.* 441 (1993) 97.
- [23] B.R. Lawn, A.G. Evans, *J. Mater. Sci.* 12 (1977) 2195.
- [24] X. Chen, J.W. Hutchinson, A.G. Evans, *J. Am. Ceram. Soc.* 88 (2005) 1233–1238.
- [25] M. Watanabe, T. Xu, A.G. Evans, *Acta Mater.* 53 (2005) 3765.
- [26] C.M. Preece, *Erosion: Treatise on Materials Science and Technology*, vol. 16, Academic Press, NY, 1979.